Bow Echo Mesovortices. Part II: Their Genesis

NOLAN T. ATKINS AND MICHAEL ST. LAURENT

Lyndon State College, Lyndonville, Vermont

(Manuscript received 13 May 2008, in final form 3 November 2008)

ABSTRACT

This two-part study examines the damaging potential and genesis of low-level, meso-γ-scale mesovortices formed within bow echoes. This was accomplished by analyzing quasi-idealized simulations of the 10 June 2003 Saint Louis bow echo event observed during the Bow Echo and Mesoscale Convective Vortex Experiment (BAMEX). In Part II of this study, mesovortex genesis was investigated for vortices formed at different stages of convective system evolution. During the early ''cellular'' stage, cyclonic mesovortices were observed. The cyclonic mesovortices formed from the tilting of baroclinic horizontal vorticity acquired by downdraft parcels entering the mesovortex. As the convective system evolved into a bow echo, cyclonic–anticyclonic mesovortex pairs were also observed. The vortex couplet was produced by a local updraft maximum that tilted baroclinically generated vortex lines upward into arches. The local updraft maximum was created by a convective-scale downdraft that produced an outward bulge in the gust front position. Cyclonic-only mesovortices were predominantly observed as the convective system evolved into the mature bow echo stage. Similar to the early cellular stage, these mesovortices formed from the tilting of baroclinic horizontal vorticity acquired by downdraft parcels entering the mesovortex. The downdraft parcels descended within the rear-inflow jet. The generality of the mesovortex genesis mechanisms was assessed by examining the structure of observed mesovortices in Doppler radar data. The mesovortex genesis mechanisms were also compared to others reported in the literature and the genesis of low-level mesocyclones in supercell thunderstorms.

1. Introduction

It has long been recognized that bow echoes can be prolific producers of straight-line wind damage and tornadoes. Early studies combining radar and damage survey data suggested that the straight-line wind damage swaths were produced by a rear-inflow jet (RIJ) descending to the ground from the rear, near the apex of the developing bow echo (e.g., Fujita 1978). Doppler radar studies have since provided corroborating evidence linking the descending RIJ to straight-line wind damage swaths (e.g., Forbes and Wakimoto 1983; Schmidt and Cotton 1989; Burgess and Smull 1990; Jorgensen and Smull 1993; Przybylinski 1995; Funk et al. 1999; Atkins et al. 2004).

Recent studies, however, have highlighted the important role that mesovortices often play in the production of straight-line wind damage within bow echoes. Mesovortices are meso-γ-scale (Orlanski 1975) circulations formed at low levels on the bow echo gust front. Observational studies (e.g., Atkins et al. 2005; Wakimoto et al. 2006b; Wheatley et al. 2006) have shown that straight-line wind damage swaths containing F0–F1 surface wind damage were created by bow echo mesovortices near or just north of the bow echo apex. Wakimoto et al. (2006b) showed that the damaging near-surface winds were generated by a superposition of the vortex and system flow within which the mesovortex was embedded. This result was also observed in quasi-idealized bow echo simulations presented in the first part of this study (Atkins and St. Laurent 2009, hereafter Part I).

Mesovortices have also been observed to produce tornadoes (e.g., Forbes and Wakimoto 1983; Wakimoto 1983; Przybylinski 1995; Funk et al. 1999; Przybylinski et al. 2000; Atkins et al. 2004, 2005). Most bow echo tornadoes produce F0–F2 surface wind damage and have relatively short damage swath lengths. Regardless of whether a mesovortex produces straight-line or tornadic wind damage, an important observation is that the

Corresponding author address: Nolan T. Atkins, Department of Meteorology, Lyndon State College, 1001 College Rd., Lyndonville, VT 05851.
E-mail: nolan.atkins@lyndonstate.edu

DOI: 10.1175/2008MWR2650.1

most intense damage within a bow echo may be associated with mesovortices (e.g., Atkins et al. 2005; Wakimoto et al. 2006b; Wheatley et al. 2006).

Given the important role that mesovortices play in the production of damaging surface winds, understanding how they form and their damaging potential are important considerations in the detection and warning processs. In Part I of this study, the damaging potential was investigated in a series of sensitivity experiments. Stronger mesovortices formed when the low-level shear was nearly balanced by the cold pool and as the magnitude of deeper-layer shear increased. Larger Coriolis forcing and stronger cold pools also produced stronger mesovortices. It was also observed that the strongest ground-relative winds were produced by mesovortices formed near the descending rear-inflow jet (RIJ). The strong surface winds were created by the superposition of the RIJ and mesovortex flows and were located on the southern flank of the mesovortex.

The genesis of bow echo mesovortices has received little attention in the literature. Through analysis of idealized simulations, Trapp and Weisman (2003) showed that convective-scale rainy downdrafts tilted horizontal vorticity that was baroclinically generated across the gust front. The tilted vortex lines (lines tangent to the vorticity vector) produced cyclonic–anticyclonic vertical vorticity couplets with the anticyclonic member located to the north of the cyclonic circulation. Convergence of planetary vorticity enhanced the cyclonic mesovortex and weakened the anticyclonic circulation. Wheatley and Trapp (2008) analyzed a simulation of the 6 July 2003 Omaha, Nebraska, bow echo event observed during the Bow Echo and Mesoscale Convective Vortex Experiment (BAMEX) and documented mesovortex pairs produced by the mechanism described by Trapp and Weisman (2003). A similar genesis mechanism was discussed by Wakimoto et al. (2006b) for the 6 July 2003 event. Their analysis of dual-Doppler airborne radar observations of a damaging mesovortex showed that mechanically forced downdrafts tilted baroclinically generated vortex lines behind the bow echo gust front to create cyclonic–anticyclonic mesovortex pairs, similar to those documented by Trapp and Weisman (2003).

Not all observational studies, however, have shown the existence of mesovortex couplets near the time of genesis. Single-Doppler studies by Atkins et al. (2004, 2005) and Wheatley et al. (2006) documented cyclonic-only mesovortices at or near the time of genesis. This result was also observed by Wakimoto et al. (2006b) in a flight leg of dual-Doppler airborne radar data for a damaging bow echo event observed on 23 June 2003 over much of Iowa. Other studies have highlighted the role of preexisting boundaries intersecting the primary convective system (e.g., Klimowski et al. 2000; Przybylinski et al. 2000; Schmocker et al. 2000) where cyclonic-only mesovortices were observed to form at the intersection point. A number of studies have implicated shearing instability (Miles and Howard 1964) as the genesis mechanism for cyclonic only low-level vortices formed along other mesoscale boundaries such as gust fronts (e.g., Carbone 1982; Mueller and Carbone 1987; Lee and Wilhelmson 1997), the dryline (Murphey et al. 2006; Marquis et al. 2007), cold fronts (Arnott et al. 2006), and the Denver convergence zone (Wakimoto and Wilson 1989). Wheatley and Trapp (2008) suggested that shearing instability produced mesovortices observed within a cool-season squall-line bow echo.

Based on the foregoing discussion, there is no clear conceptual model of mesovortex genesis that is consistent among modeling and observational studies. The primary objective of this second part of the study is, therefore, to better understand the genesis mechanism(s) of bow echo mesovortices. This will be accomplished by analyzing quasi-idealized simulations of the 10 June 2003 bow echo documented by Atkins et al. (2005).

This paper is organized as follows: The experimental design is discussed in section 2. Section 3 presents an overview of the control run while section 4 details the mesovortex genesis mechanisms. Conclusions are summarized in section 5.

2. Experimental design

As in Part I, the Advanced Research Weather Research and Forecasting (ARW-WRF) model (Skamarock et al. 2005) was used to generate a quasi-idealized simulation of the 10 June 2003 Saint Louis bow echo event. Computations were carried out on a model grid that was 200 and 300 km in size in the west–east and north–south directions, respectively. The model was initialized with the 1800 UTC sounding launched at Springfield, Missouri, on 10 June 2003 (see Fig. 1 in Part I). Storm motion was subtracted from the base-state winds to ensure that the convective system would stay in the middle of the model domain for the entire 6-h simulation. The domain extended up to 17.25 km in the vertical direction. The horizontal grid spacing was 500 m, slightly better than the 750-m horizontal grid spacing used in Part I. The vertical grid spacing varied from 160 m near the ground to 600 m near the model top. These horizontal and vertical grid resolutions well resolved the mesovortex genesis mechanisms. The lateral boundary conditions were open. The upper and lower boundaries were rigid. A Rayleigh damping layer was placed above 12 km to suppress wave motions above the tropopause. The lower boundary condition was free slip. It is acknowledged

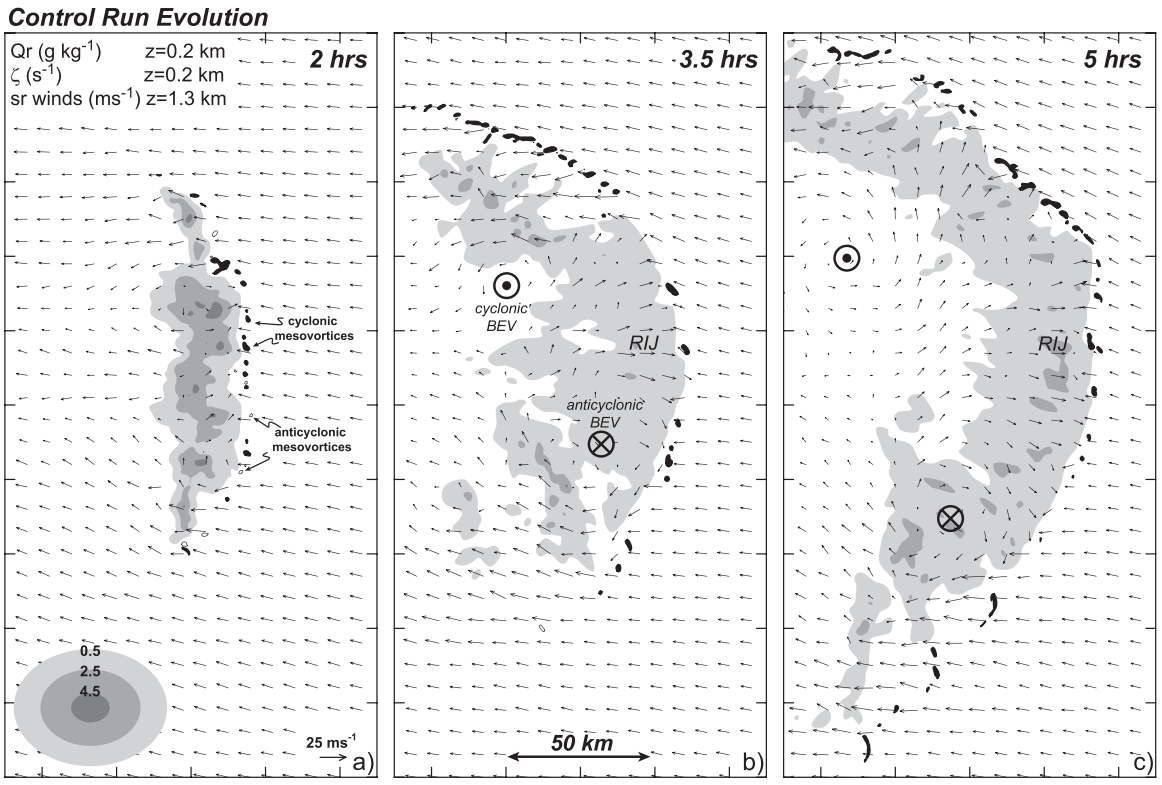

FIG. 1. Evolution of the control run at 2, 3.5, and 5 h into the simulation. Rainwater mixing ratio (g kg^{-1}) is shaded gray. Locations of cyclonic mesovortices where the vertical vorticity is greater than 1.25×10^{-2} s^{-1} are filled in black. The thin black contours are locations of anticyclonic mesovortices having vertical vorticity values less than -1.25×10^{-2} s^{-1}. The positions of the cyclonic and anticyclonic bookend vortices are shown at 3.5 and 5 h. Storm-relative winds (m s^{-1}) at 1.3 km are plotted at all times.

that the lack of surface friction will have some impact on the low-level wind field. While previous investigators (e.g., Lee and Wilhelmson 1997) have noted that frictional effects are important for simulating small-scale vortices such as tornadoes, the results of Adlerman and Droegemeier (2002) and Weisman and Trapp (2003), however, suggest that the structural evolution of meso-γ-scale circulations such as mesovortices was not significantly impacted by the exclusion of surface friction. Convection was initiated in the model domain with three thermal bubbles 20 km apart oriented in the north–south direction. The Coriolis parameter was set to 1×10^{-4} s^{-1} and acted only on the wind perturbations. The 1.5-TKE closure scheme available in WRF was used to parameterize subgrid-scale turbulence while the Lin et al. (1983) ice microphysics scheme was employed to parameterize microphysical processes.

3. Overview of the control run

An overview of the simulated convective system is shown in Fig. 1. The three thermal bubbles used to initiate convection had produced a north–south-oriented linear convective line by 2 h (Fig. 1a). On the gust front, cyclonic and anticyclonic mesovortices had formed. The convective system evolved into a bow echo over the next 1.5 h (Fig. 1b). The convective system has bowed out in response to the development of a RIJ that was observed in the storm-relative wind field at 1.3 km. Cyclonic and anticyclonic bookend vortices (Weisman 1993) were also observed on the northern and southern ends of the bow echo. The bookend vortices have been shown to form by the upward tilting by the system-scale updraft of horizontal vortex lines that were baroclinically generated just behind the bow echo gust front (Weisman and Davis 1998). On the bow echo gust front, cyclonic-only mesovortices were observed and appeared to be larger in size than those observed earlier in the simulation. The increased size was due to the merging of liked-signed mesovortices (not shown), a behavior also observed by Trapp and Weisman (2003). By 5 h into the simulation, the entire convective system had grown upscale. The cyclonic bookend vortex had propagated rearward relative to the leading edge of the convective system. Cyclonic-only mesovortices were again observed on the bow echo gust front.

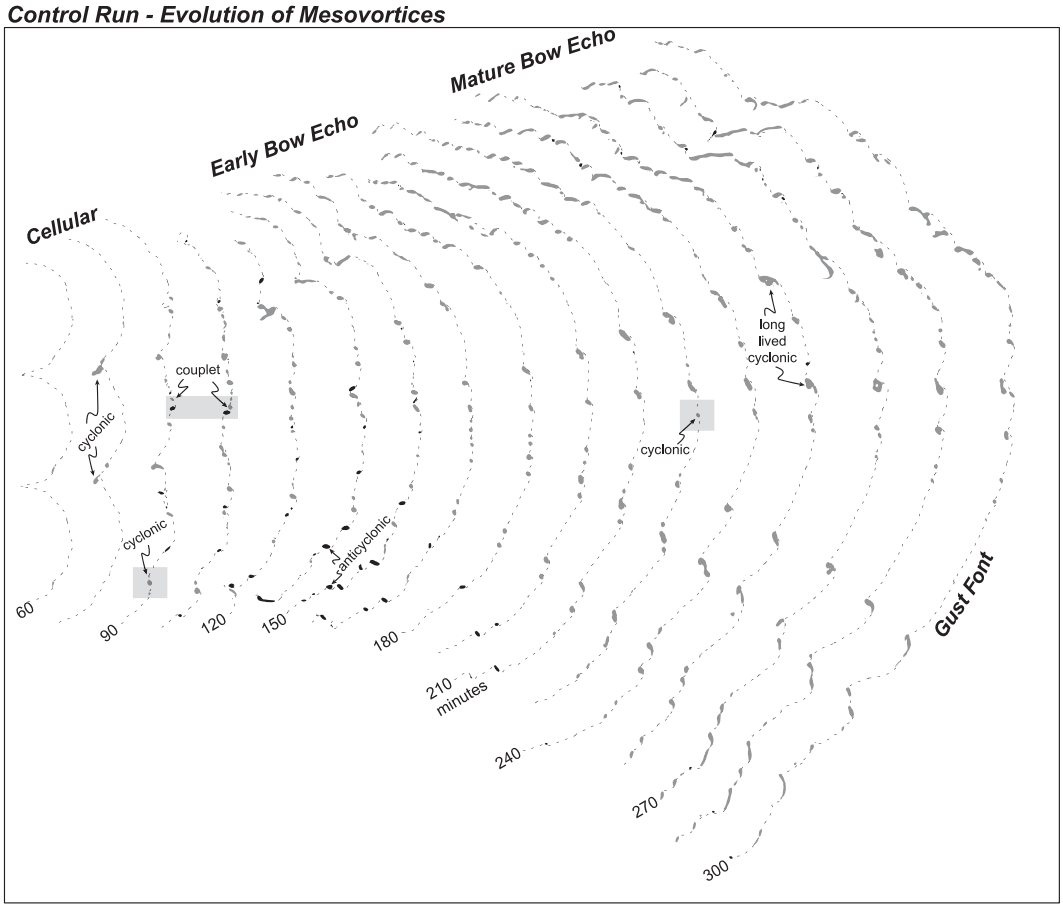

FIG. 2. Gust front (dashed lines) and mesovortex locations are plotted from 60 to 360 min, every 15 min at 0.2 km. The gust front position delineates the eastern edge of the cold pool defined as the −1°C perturbation from the base state at 0.2 km. Cyclonic and anticyclonic mesovortex locations are filled gray and black, respectively, and are defined in a similar manner as in Fig. 1. Gray boxes highlight mesovortices that will be analyzed in subsequent figures.

A more detailed depiction of mesovortex evolution is shown in Fig. 2 where the gust front and mesovortex positions are shown every 15 min. During the early ''cellular'' stage, the convective system was composed of storms formed from the initial thermal bubbles. In fact, three individual ouflows were apparent in the gust front position at 60 and 75 min. During this stage, cyclonic-only mesovortices were observed along the gust front. As the convective system continued to evolve and began to acquire bow echo characteristics (early bow echo stage), both cyclonic-only and mesovortex couplets were observed to form. Couplets can be seen at 90 and 105 min. In contrast with the results of Trapp and Weisman (2003) and Wheatley and Trapp (2008), however, the couplets formed in the control simulation have the cyclonic member to the north, suggesting a different genesis mechanism than that proposed by Trapp and Weisman (2003). As the convective system evolved into the mature bow echo stage, cyclonic-only mesovortices were observed. The mature stage was defined where the bow echo began to acquire asymetric structure as the cyclonic bookend vortex became larger and stronger than the southern anticyclonic circulation due to the convergence of planetary vorticity (Skamarock et al. 1994). Many of these mesovortices were long-lived circulations that had formed during the early bow echo stage. Others, however, formed later during the mature bow echo stage.

The results in Fig. 2 suggest that the mesovortex genesis mechanisms may be different than those reported in Trapp and Weisman (2003). First, Trapp and Weisman (2003) only observed couplets during the time of genesis. In contrast, cyclonic-only mesovortices were observed to form primarily during the early cellular and mature stages in Fig. 2. Second, the couplets reported by Trapp and Weisman (2003) formed by downdrafts tilting horizontal vortex lines solenoidally generated behind the gust front producing an anticyclonic circulation

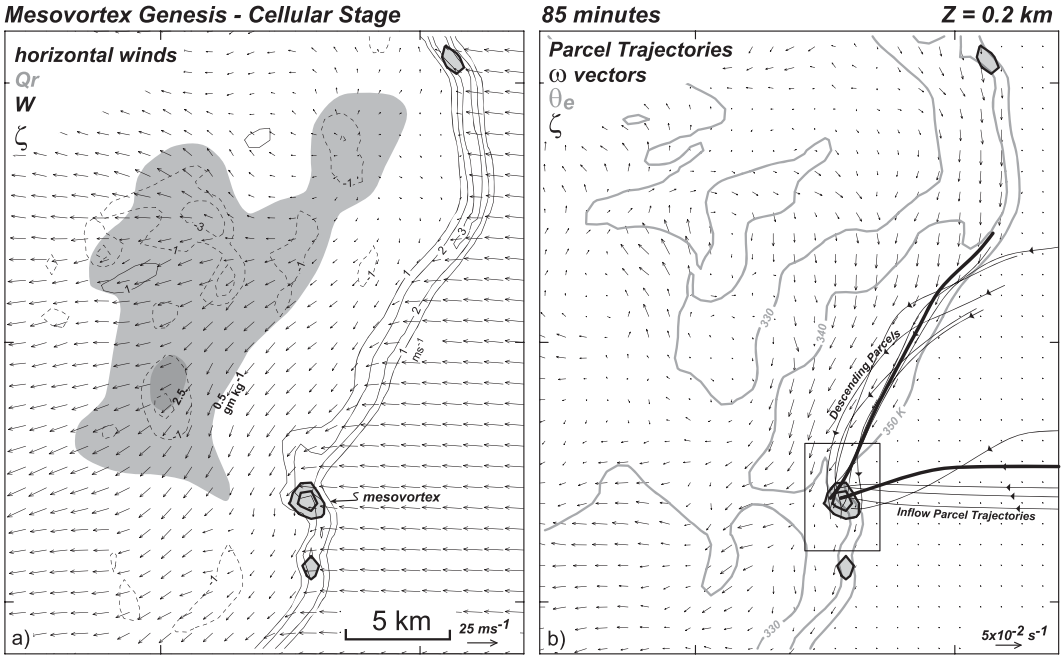

FIG. 3. Analysis of mesovortex genesis during the cellular stage. The analyzed mesovortex is highlighted in the gray box in Fig. 2 at 90 min. (a) Rainwater mixing ratio (g kg^{-1}) is plotted in gray. Vertical velocity (m s^{-1}) is contoured with thin dashed (negative) and solid (positive) contours. Thick solid contours are vertical vorticity beginning and incremented at 1×10^{-2} s^{-1}. Horizontal wind vectors are also shown. (b) Equivalent potential temperature (K) is plotted in gray. Air parcel trajectories projected to 0.2 km are shown as solid black lines. The vector field is horizontal vorticity. Vertical vorticity is plotted as in (a). The box represents the area shown in Fig. 5a. All fields in both (a) and (b) are plotted at 0.2 km.

to the north. The couplets observed primarily during the late cellular and early bow echo stages in Fig. 2 clearly show the cyclonic member north of the anticyclonic circulation. It should be noted that the low-level environmental shear was slightly stronger in the Trapp and Weisman (2003) simulations than in the control run shown in Fig. 2. In the next section, the geneses of the cyclonic-only and mesovortex couplets observed in the control run are discussed in detail.

4. Mesovortex genesis mechanisms

a. Cyclonic-only mesovortices during the cellular stage

The genesis of the cyclonic mesovortex highlighed in the gray box at 90 min in Fig. 2 is now shown. It is representative of the other cyclonic mesovortices formed during the cellullar stage. A more detailed depiction of this mesovortex is shown in Fig. 3. The vortex was located on the southeastern flank of a convective cell, evident in the rainwater mixing ratio field. This cell was located on the southern end of the convective line and exhibited transient supercellular characteristics. Supercellular structures were also observed in idealized bow echo simulations by Weisman (1993) before the cold pool became dominant. The mesovortex in Fig. 3a was embedded in updraft along the gust front. Figure 3b illustrates that it was also located on the gradient of equivalent potential temperature (θ_e) and suggested that the air feeding the mesovortex was coming from both the high θ_e inflow and the lower θ_e air behind the gust front. To further illustrate this point, backward parcel trajectories were computed for parcels populating the mesovortex at 85 min. The near-surface positions of these trajectories are shown in Fig. 3b. Mesovortex parcels were coming from the storm-relative inflow at low levels. Many other parcels entered the mesovortex from the north, behind the gust front. These parcels were descending to low levels before entering the mesovortex and originated in the convective-cell downdraft to the northwest of the mesovortex.

Two approaches were taken to understand the genesis of the mesovortex in Fig. 3. The first involved analysis of the vorticity equation. For inviscid, Boussinesq flow, the three-dimensional vorticity equation can be written as

$$\frac{d\boldsymbol{\omega}}{dt} = (\boldsymbol{\omega} + f\mathbf{k}) \cdot \nabla\mathbf{V} + \nabla \times (B\mathbf{k}), \qquad (1)$$

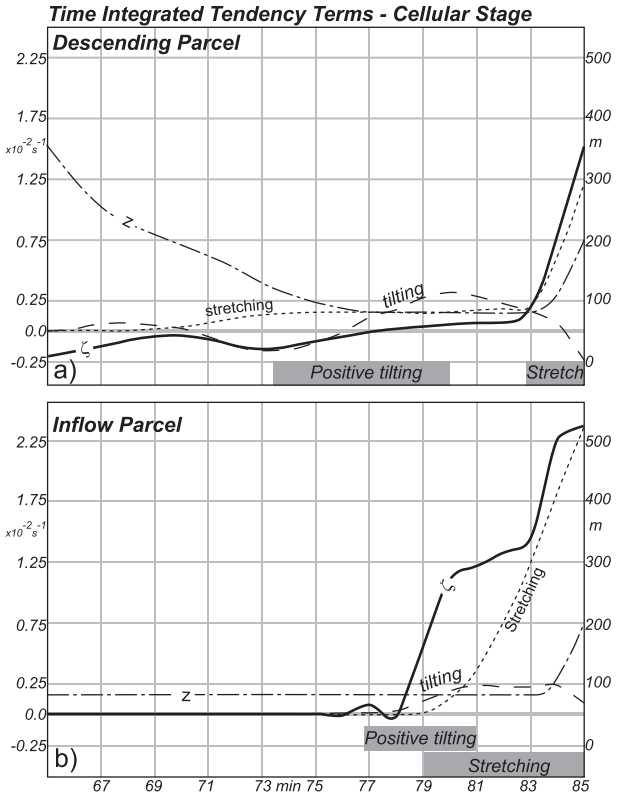

FIG. 4. Time series of integrated vertical vorticity tendency terms (s^{-1}) for (a) a descending parcel and (b) an inflow parcel. The parcel vertical vorticity (s^{-1}) and height (m) are also plotted. Trajectory locations for both parcels are shown as thick black lines in Fig. 3b.

where $\boldsymbol{\omega}$ and $\mathbf{V}$ are the three-dimensional vorticity and velocity vectors, respectively; f is the Coriolis parameter; $\mathbf{k}$ is the vertical unit vector; and B is buoyancy. The mixing term has been omitted from this analysis. Physically, the first term on the right-hand side of (1) represents the change of the vorticity vector due to tilting and stretching while the second term represents the production of vorticity due to a horizontal buoyancy gradient. As the generation of mesovortices involves the production of vertical vorticity, the vertical component of (1) is given by

$$\frac{d\zeta}{dt} = \boldsymbol{\omega}_H \cdot \nabla_H w + (\zeta + f)\frac{\partial w}{\partial z}, \tag{2}$$

where ζ is the vertical component of vorticity and w is the vertical velocity. The terms on the right-hand side of (2) represent the change of vertical vorticity due to tilting of horizontal and stretching of vertical vorticity, respectively. As Trapp and Weisman (2003) showed that convergence of planetary vorticity played an imporant role in mesovortex evolution, the tendency of absolute vertical vorticity ζ_a ($=\zeta + f$) will be examined.

The tilting and stretching tendency terms were integrated along representative parcel trajectories in order to determine how parcels acquired absolute vertical vorticity according to

$$\zeta_a(x, y, z, t) = \zeta_a(x_o, y_o, z_o, t_o) + \int_{t_o}^{t} \boldsymbol{\omega}_H \cdot \nabla_H w dt + \int_{t_o}^{t} \zeta_a \frac{\partial w}{\partial z} dt. \tag{3}$$

Model output data every one minute from 65 to 85 min was used to calculate the time-integrated tilting and stretching terms along with ζ_a. The absolute vertical vorticity calculated from (3) was in close agreement with the observed value of ζ_a along the parcel path (not shown). The results of this integration for representative descending and inflow parcels are shown in Fig. 4. Initially, the descending parcel (bold parcel path behind the gust front in Fig. 3b) was located at 1.5 km and descended to 0.25 km by 77 min. In doing so, the parcel encountered positive tilting just after 73 min. While not plotted in Fig. 4, it was clear in looking at the parcel trajectory paths and horizontal vorticity field in Fig. 3b that the descending parcels acquired streamwise horizontal vorticity as they approached the developing mesovortex. The positive tilting of horizontal streamwise vorticity lasted until 80 min and generated weak positive vertical vorticity. The weak positive vertical vorticity was then amplified quickly through vortex stretching by the updraft along the gust front after 83 min.

At 65 min, the inflow parcels originated at $z = 0.2$ km. A representative parcel is shown in Fig. 4b (ground path shown as thick black line in Fig. 3b). As it approached the mesovortex, it encountered positive tilting at 77 min. Similar to the descending parcel, the inflow parcel contained positive streamwise horizontal vorticity, however, the magnitude was much smaller (not shown) than for the descending parcels. The positive tilting after 77 min generated positive vertical vorticity that was further amplified through vortex stretching after 79 min. The much smaller magnitude of the horizontal vorticity field within the inflow than what was observed behind the gust front in Fig. 3b suggested that the descending, low θ_e, parcels appeared to be most important in generating the mesovortex through the tilting of horizontal streamwise vorticity.

Following the discussion in Rotunno and Klemp (1985), the genesis process was also investigated through analysis of the circulation of a material curve within a fluid. The circulation $C(t)$ is defined as

$$C(t) = \oint (\mathbf{V} \cdot dl), \tag{4}$$

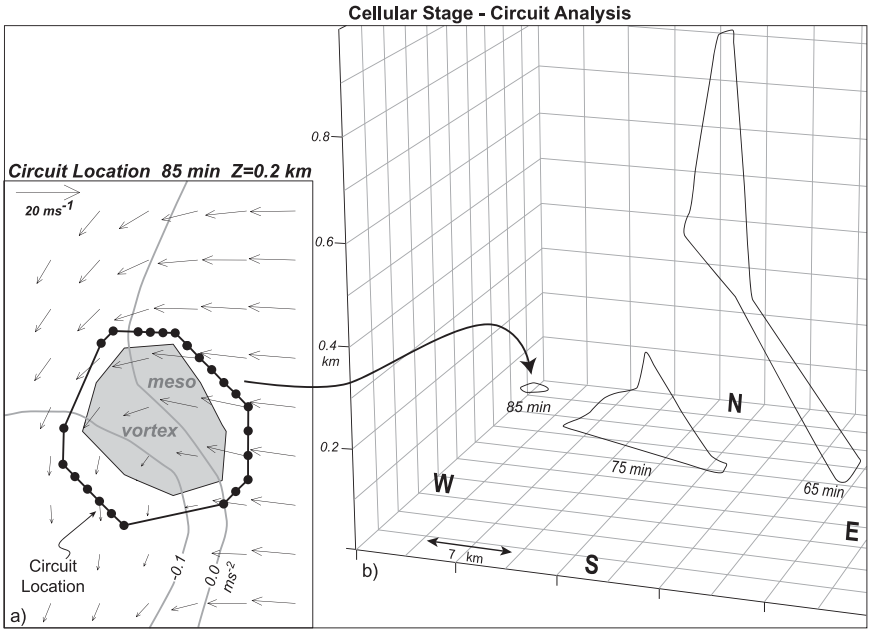

FIG. 5. (a) Location of mesovortex in Fig. 3b is shaded gray. Gray contours are buoyancy ($m\ s^{-2}$) while horizontal winds ($m\ s^{-1}$) are shown as the vector field. The initial circuit of parcel locations surrounding the mesovortex is shown as the solid black contour. Parcel positions are shown as black dots. All fields are plotted at 0.2 km. (b) Three-dimensional perspective of the circuit position at 65, 75, and 85 min into the simulation.

where **V** is the three-dimensional velocity vector and the integration is performed around a closed material surface (e.g., Batchelor 1967). The change in circulation with time following the closed material surface, assuming the inviscid Bousinesq approximation, is given by Bjerknes's first circulation theorem (Eliassen and Kleinschmidt 1957) as

$$\frac{dC}{dt} = \oint (B\mathbf{k} \cdot dl), \tag{5}$$

where B is buoyancy. Thus, circulation around a material surface may change with time because of buoyancy effects. The relationship between circulation and vorticity can be seen by applying Stokes theorem to (4), which yields

$$\frac{dC}{dt} = \int_A \nabla \times (B\mathbf{k}) \cdot dA, \tag{6}$$

where the integration is over a sufficiently well-behaved area bounded by the material surface. The integrand represents the solenoidal generation term in (1). Therefore, the circulation tendency is related to the vortex lines that are solenoidally generated and pass through the material surface (Trapp and Fiedler 1995).

A material surface was placed around the mesovortex in Fig. 3 and is shown in Fig. 5. Notice that a portion of the mesovortex was positioned within negatively buoyant air (Fig. 3b) that descended from aloft in the convective-scale downdraft. This can also be seen in Fig. 5b where the three-dimensional material surface location was plotted at 85, 75, and 65 min. At 65 min, the northern portion of the material surface was located at altitudes exceeding 0.8 km; however, the inflow portion of the material surface was located at low levels well to the east. By 75 min, most of the material surface was near the ground. As the descending and inflow parcels converged toward the final mesovortex position, the material

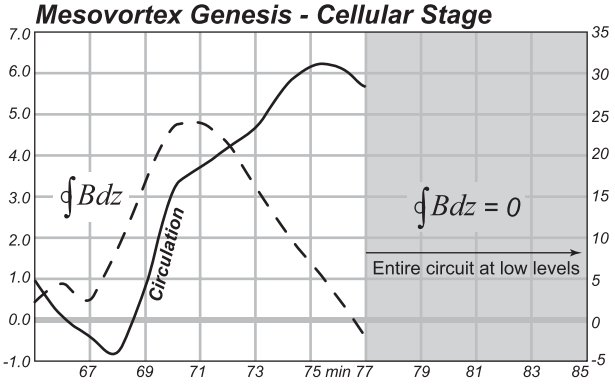

FIG. 6. Time series of circulation tendency (dashed line) and circulation (solid line) calculated around the circuit shown in Fig. 5 from 65 to 77 min. After 77 min, the entire circuit was at low levels.

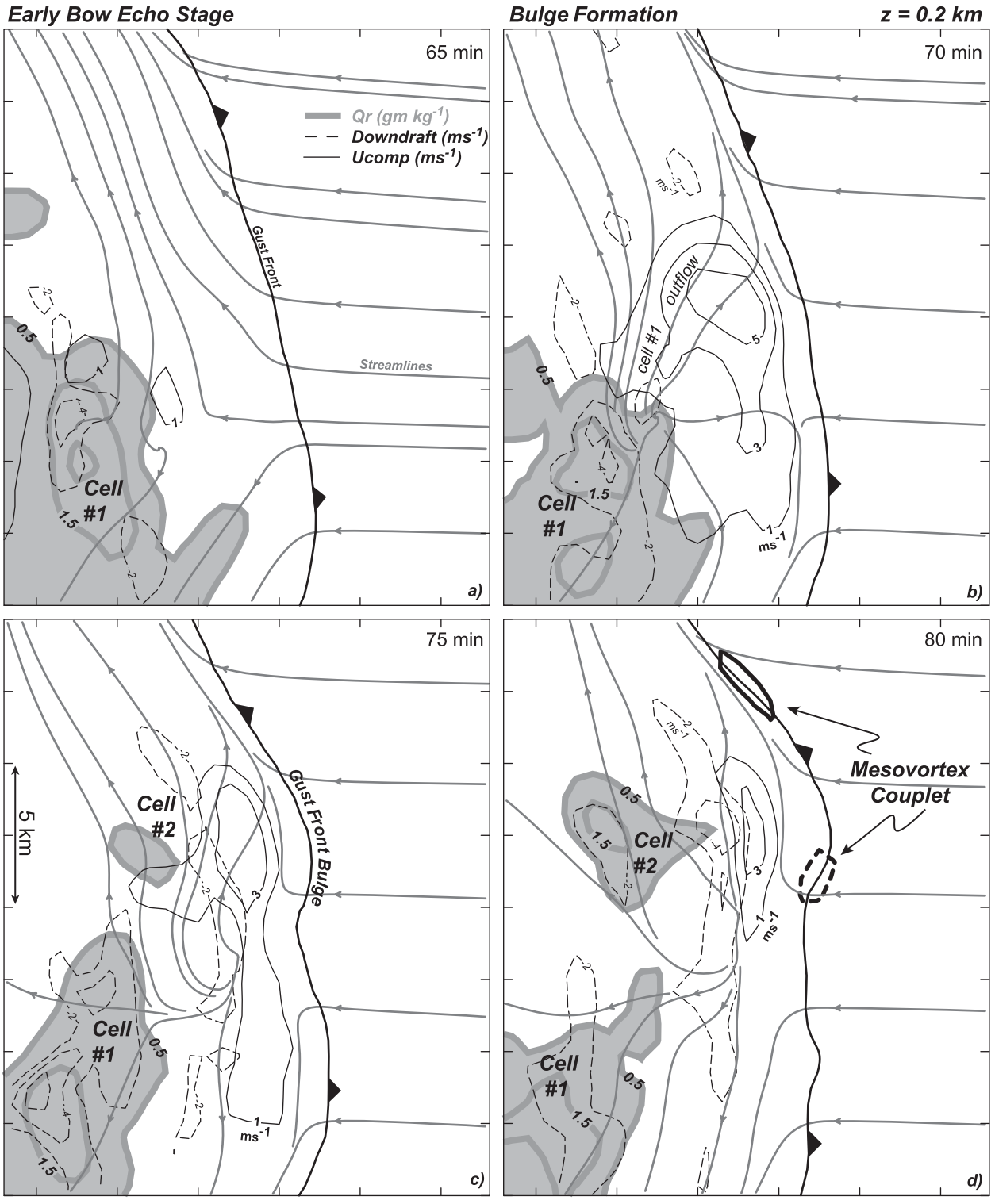

FIG. 7. Time series of horizontal streamlines (thin gray lines), rainwater mixing ratio (thick gray contours; g kg^{-1}), storm relative U component (thin black lines; m s^{-1}), and gust front position (thick black line) at (a) 65, (b) 70, (c) 75, and (d) 80 min. The thick black solid and dashed contours in (d) are positive and negative vertical vorticity, respectively. All fields are plotted at $z = 0.2$ km.

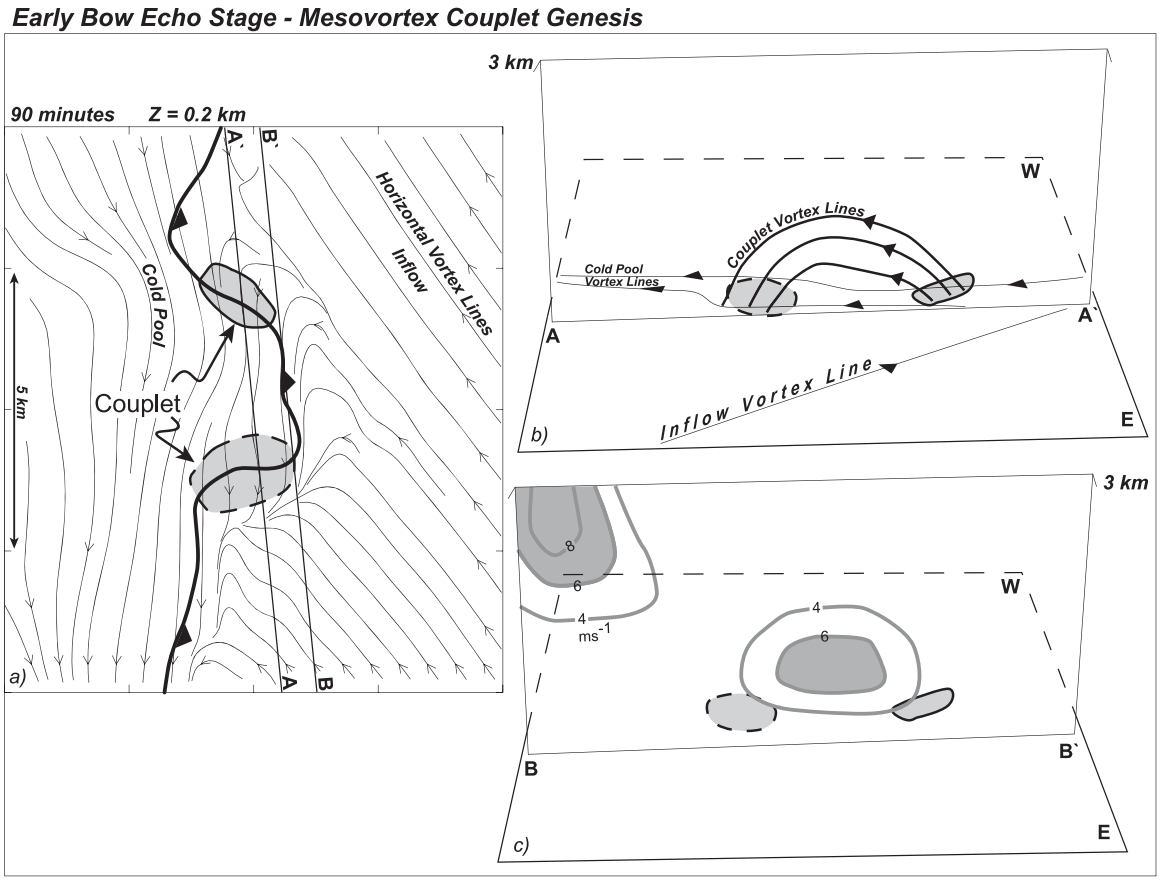

FIG. 8. (a) Plan view of horizontal vortex lines, vertical vorticity, and gust front position at $z = 0.2$ km, 90 min into the simulation. The analyzed mesovortex couplet is also shown at 90 and 105 min in Fig. 2 and 80 min in Fig. 7. Positive and negative vertical vorticity are plotted as solid and dashed black contours filled with gray. Only the 1×10^{-2} s^{-1} vertical vorticity contour was plotted to highlight mesovortex positions. (b) Plan-view and vertical cross section through the mesovortex couplet are shown in (a). The inflow and cold-pool vortex lines and vertical vorticity contours are all plotted at $z = 0.2$ km on the plan-view cross section. Thick black lines are vortex lines in the plane of the vertical cross section and pass through the cyclonic and anticyclonic mesovortices. Cross-section location is shown in (a). (c) As in (b), except that the vertical cross section is farther to the east; the location is shown in (a). Vertical velocity is contoured in gray with values greater than 6 m s^{-1} shaded.

surface had reached its final position at $z = 0.2$ km by 85 min. Equation (5) was integrated around the the material surface using model output data every 1 min beginning at 65 min. As shown in Fig. 6, the circulation tendency was positive from 65 to 77 min. The circulation computed from model data around the material surface increases from 68 min to approximately 76 min. When the material surface was entirely at the same vertical level, as was the case after 77 min, the circulation tendency was zero. Thus, consistent with the vorticity equation analysis, analysis of circulation about a material surface surrounding the mesovortex illustrated the important role of the low θ_e air descending from the convective-scale downdrafts in mesovortex genesis. Vortex lines passing through the northern, subsiding portion of the material surface were tilted upward, generating positive circulation. Interestingly, the genesis of the mesovortex shown in Figs. 3–6 appears to be similar to what was originally discussed by Rotunno and Klemp (1985) for the genesis of low-level mesocyclones in supercell thunderstorms.

b. Mesovortex couplets during the late cellular and early bow echo stages

In addition to the cyclonic mesovortics, cyclonic–anticyclonic vortex pairs, or couplets, were observed to form primarily during the late cellular and early bow echo stage of convective system evolution. In contrast to the results presented by Trapp and Weisman (2003) and Wheatley and Trapp (2008), the couplets produced in the control simulation have the cyclonic member located north of the anticyclonic circulation. This configuration is evident in Fig. 2 for the couplet highlighted at 90 and 105 min and was true for all others observed to

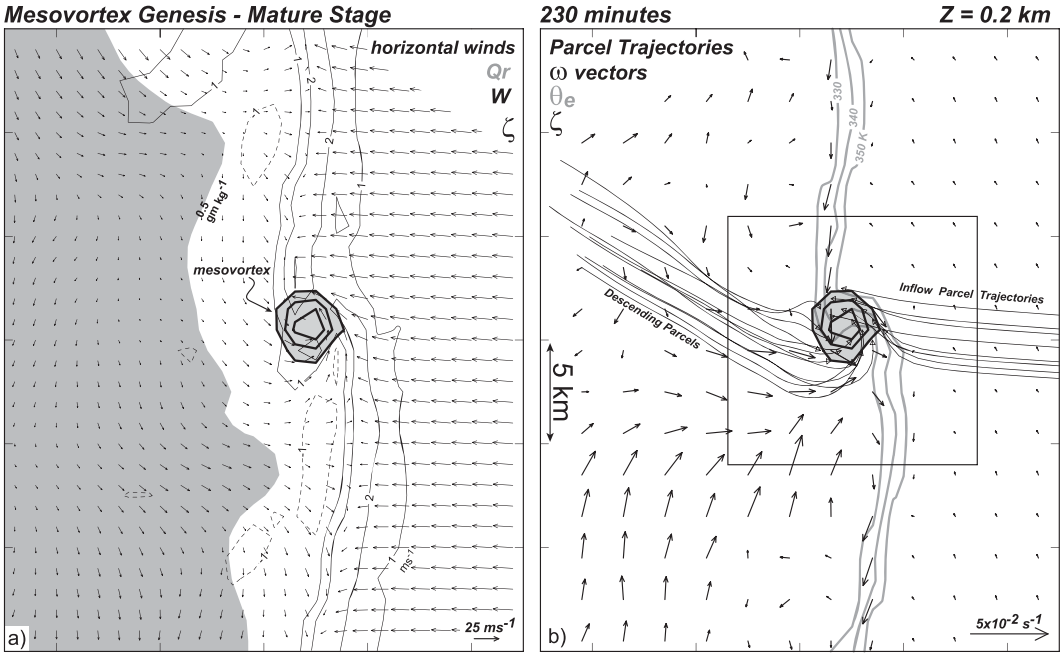

FIG. 9. As in Fig. 3, but for the highlighted mesovortex at 225 min in Fig. 2. The box in (b) represents the analysis region in Fig. 10.

form in the control simulation. An analysis of the couplet genesis is now presented.

The formation of the mesovortex couplet highlighted in Fig. 2 is shown in Fig. 7. The analysis began at 65 min (Fig. 7a) where convective cell 1 was evident in the rainwater mixing ratio field behind the gust front. Downdraft from this cell was just reaching the surface and was evident as divergent outflow at 70 min in Fig. 7b. The outflow had produced a local maximum of storm-relative westerly flow exceeding 5 m s^{-1} behind the gust front and was propagating to the northeast. The outflow continued to propagate northeast and began to impinge upon the gust front by 75 min (Fig. 7c). In doing so, the outflow had locally accelerated the gust front to the east creating a local ''bulge'' in its surface position. By 80 min (Fig. 7d), the gust front bulge was more pronounced. It is possible that outflow from convective cell 2 (Figs. 7c,d) had also contributed to the outflow that was generating the local gust front bulge. More importantly, vertical vorticity maxima were generated on either side of the gust front bulge with cyclonic and anticyclonic vertical vorticity located on the northern and southern sides, respectively.

To understand how the mesovortex couplet in Fig. 7d was produced, an analysis of vortex lines in the vicinity of the gust front bulge is presented in Fig. 8. The gust front bulge and mesovortex couplet had become more prominent at 90 min (Fig. 8a). While the vortex lines associated with the inflow were oriented to the northwest, the vortex lines passing through the couplet and behind the gust front were northerly. These northerly vortex lines were associated with horizontal vorticity that was solenoidally generated across the gust front. Two of these northerly cold-pool vortex lines were also plotted in the plan view cross section in Fig. 8b. Notice that they passed through the mesovortex couplet. Vortex lines passing through the couplet in the vertical cross section (A–A′) were also plotted and were observed to arch upward. These arching vortex lines were tilted upward by the local updraft observed at the leading edge of the gust front bulge (Fig. 8c). The updraft maximum exceeding 6 m s^{-1} was located on the gust front between the vortex couplet. Thus, it was the updraft locally tilting upward the horizontal cold-pool vortex lines into arches that in turn created the mesovortex couplet.

The analysis in Fig. 8 explains the difference between couplets formed in the control simulation and those presented by Trapp and Weisman (2003). In the control simulation, it was the local updraft at the gust front bulge that tilted cold-pool vortex lines upward to create the mesovortex pair with cyclonic vertical vorticity located to the north. The local bulge was generated by a convective-scale downdraft and associated outflow locally accelerating the gust front outward. Trapp and Weisman (2003) observed rainy downdrafts tilting cold-

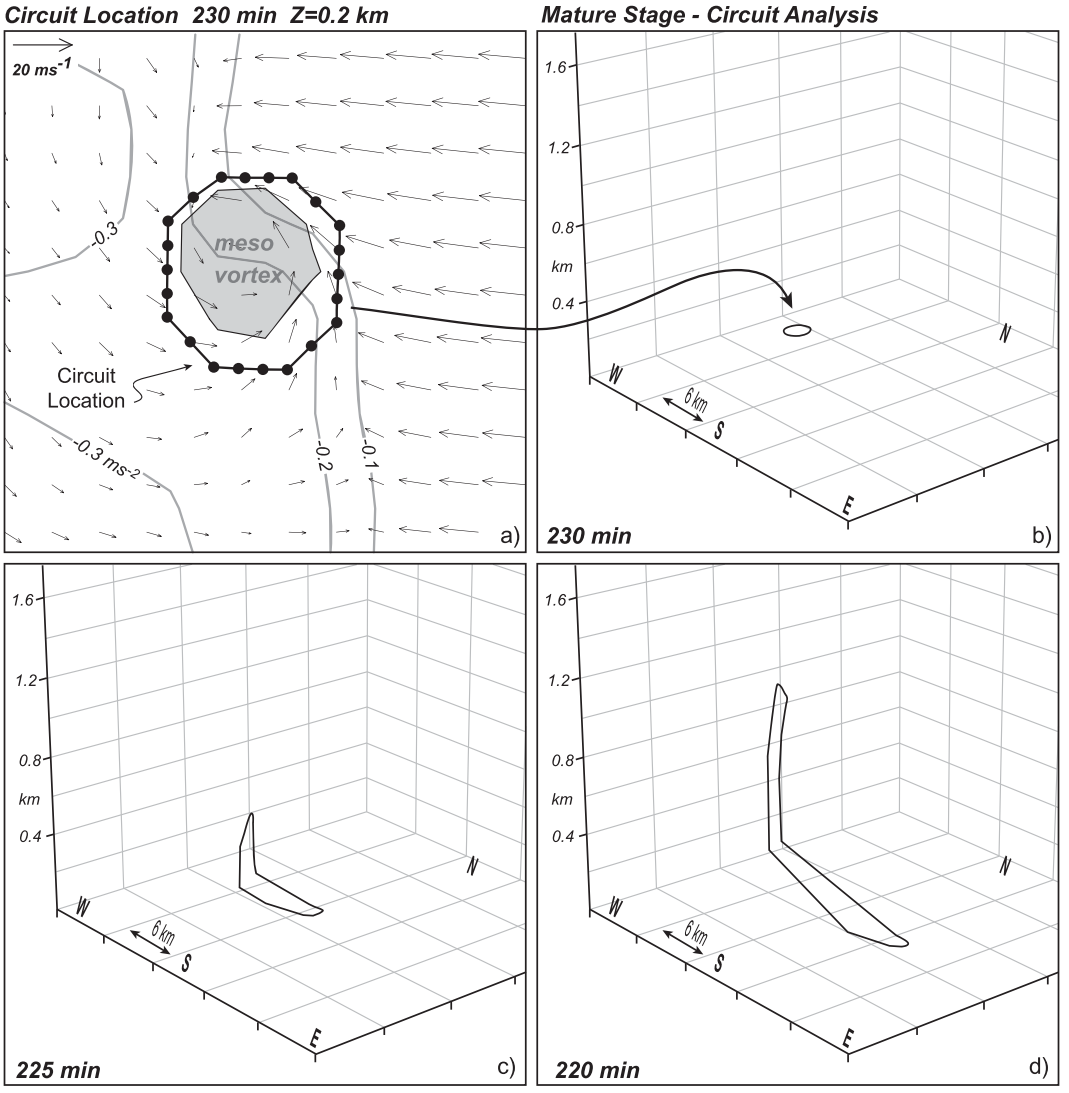

FIG. 10. (a) Location of the mesovortex in Fig. 9b is shaded gray. Gray contours are buoyancy (m s^{-2}) while horizontal winds (m s^{-1}) are shown as the vector field. The initial circuit of parcel locations surrounding the mesovortex is shown as the solid black contour. Parcel positions are shown as black dots. All fields are plotted at 0.2 km. The three-dimensional perspective of the circuit position at (b) 230, (c) 225, and (d) 220 min into the simulation.

pool vortex lines downward, creating a mesovortex pair with anticyclonic vertical vorticity to the north.

The mechanism for mesovortex couplet formation discussed in Figs. 7 and 8 is essentially the same as what has been shown to produce the larger meso-β line-end vortices by Weisman and Davis (1998). The difference is simply the scale of the updraft. Weisman and Davis (1998) noted that the system-scale updraft with a finite north–south extent was responsible for the tilting of cold-pool vortex lines on the ends of the convective system. At smaller convective scales, updraft maxima along the gust front were responsible for the meso-γ mesovortex couplets observed in the control run.

c. *Cyclonic-only mesovortices during the mature stage*

As the bow echo entered the mature stage (Fig. 2), mesovortices along the gust front were largely cyclonic. Many were long lived, having formed during the early bow echo stage. A few mesovortices, however, formed during the mature stage. An example is highlighted in Fig. 2 at 225 min. The genesis of this mesovortex is now presented.

A detailed depiction of the convective system and mesovortex highlighted at 225 min in Fig. 2 is shown in Fig. 9. The mesovortex was located within updraft (Fig. 9a)

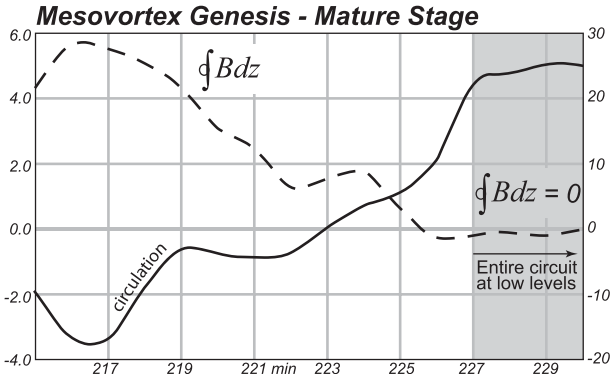

FIG. 11. Time series of circulation tendency (dashed line) and circulation (solid line) calculated around the circuit shown in Fig. 10 from 215 to 227 min. After 227 min, the entire circuit was at low levels.

and on a gradient of θ_e (Fig. 9b) along the bow echo gust front. Unlike the cellular stage, however, the rainwater mixing ratio field was much more uniform suggesting that individual convective cells were less prominent during the mature stage.

Backward parcel trajectories were again analyzed to determine where the air feeding the developing mesovortex originated. Parcels ending up in the mesovortex at 230 min were followed backward for a period of 10 min (Fig. 9b). Similar to the cyclonic mesovortex observed during the cellular stage, two source regions were apparent. One originated at low levels in the high θ_e inflow. The other was low θ_e air from the rear of the convective system within the descending RIJ. Notice that the descending parcel trajectory positions near the mesovortex were largely parallel to the horizontal vorticity vectors. This observation strongly suggests that these descending parcels acquired streamwise horizontal vorticity that was then tilted and stretched by the updraft along the gust front.

Following the discussion for the cyclonic vortex observed during the cellular stage, an analysis of a material surface surrounding the vortex in Fig. 9 is presented in Fig. 10. The mesovortex was located on a buoyancy gradient (Fig. 10a) consistent with high and low θ_e air feeding the developing vortex. The material surface in Fig. 10a surrounding the mesovortex was traced backward for a period of 10 min. The initial position at 0.2 km is shown in Fig. 10b. Five minutes earlier (Fig. 10c), the surface had become elongated in the west–east direction with the western portion located at slightly higher altitudes. At 220 min (Fig. 10c), the material surface was even more elongated. The eastern portion was located within the high θ_e inflow at low levels. The western portion of the material surface was located near 1.0 km above the surface within the descending RIJ. Following the material surface from 220 to 230 min nicely showed how parcels in these two source regions converged together into the developing mesovortex.

An analysis of the circulation tendency is shown in Fig. 11 from 215 to 230 min. While the computed circulation around the material surface was initially negative, it increased with time and became positive by 223 min. It continued to increase until 227 min at which time it was constant. After 227 min, the material surface was entirely at the same vertical level and therefore, the circulation should not change with time as shown in (4). The circulation tendency was positive at all times prior to approximately 226 min. As the entire circuit approached low levels, the tendency became zero. Thus, the genesis mechanism for the cyclonic vortex formed during the mature bow echo stage was the same as what was observed during the early cellular stage. The only difference is that during the cellular stage, the low θ_e air feeding the cyclonic mesovortex originated within a convective-scale downdraft, whereas during the mature stage, the low θ_e air originated within the descending RIJ.

d. Shearing instability as a mechanism for mesovortex genesis

The growth of perturbations along a shear zone, or vortex sheet, results in the conversion of background kinetic energy to eddy kinetic energy within the shear zone. This ''shearing instability'' (Batchelor 1967) results in a concentration of vorticity at discrete centers within the shear zone. Linear theory presented by Miles and Howard (1964) indicates that the fastest-growing mode should occur on a scale of 7.5 times the shear zone width. Many investigators have used this criteria to conclude that shearing instability may be occurring in a variety of mesoscale frontal zones including gust fronts (e.g., Carbone 1982; Mueller and Carbone 1987; Lee and Wilhelmson 1997; Wheatley and Trapp 2008), the dryline (Murphey et al. 2006; Marquis et al. 2007), cold fronts (Arnott et al. 2006), and the Denver convergence zone (Wakimoto and Wilson 1989). In many of these studies, the environment contained preexisting ambient horizontal shear that was not present in the control run initial condition. Given that cyclonic-only mesovortices formed during portions of the control run, however, it is fair to question whether shearing instability played a role in their genesis.

The potential for shearing instability was assessed by plotting the locations of mesovortex genesis every 5 min from 1 to 5 h into the simulation (Fig. 12). A grid with spacing equal to 7.5 times the shear zone width has been superimposed on the figure to facilitate comparison between theory and the simulation results. When examining the genesis locations, the majority of vortices were not forming at regular intervals along the gust front with

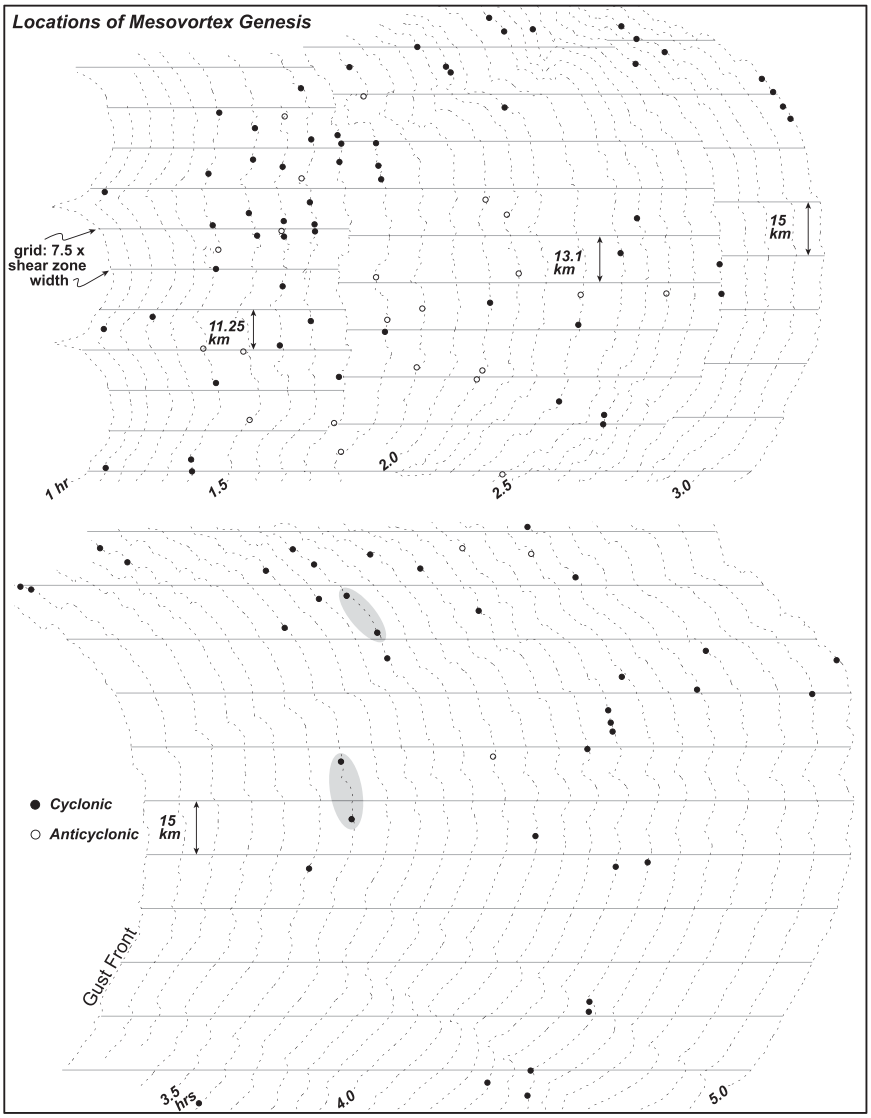

FIG. 12. Time series of gust front position (dashed) from 1 to 5 h, every 5 min. Black dots and open circles denote cyclonic and anticyclonic mesovortex genesis locations, respectively. Gray lines are spaced at 7.5 times the shear zone width at the respective times. Shaded locations represent mesovortex genesis locations that have a spacing of approximately 7.5 times the shear zone width.

a spacing predicted by linear theory. In fact, the pattern of genesis locations appeared to be quite irregular. Pairs of vortices at 3 h 40 min and 3 h 50 min (highlighted gray) were spaced at approximately 7.5 times the shear zone width. It should be noted that the southern vortex associated with the pair at 3 h 40 min is the vortex analyzed in the section 4c. Thus, the highlighted pair at 3 h, 40 min was likely not produced by shearing instability. Based on the results in Fig. 12, shearing instability was likely not involved in the genesis of the mesovortices formed within the control run.

e. Comparison with observations

In an effort to determine the applicability of the mesovortex genesis mechanisms reported herein to observed mesovortices, three bow echo events that have been studied in the refereed literature were examined. They are the 29 June 1998 (Atkins et al. 2004), 10 June 2003 (Atkins et al. 2005), and 6 July 2003 (Wakimoto et al. 2006a,b; Wheatley et al. 2006) events. All three bow echoes were progressive (Johns and Hirt 1987) warm season events that produced damaging mesovortices. Available Doppler

TABLE 1. Observed bow echo events with mesovortices.

Event	Stage of evolution	No. of vortices	Cyclonic/couplets
29 Jun 1998	Early bow echo	4	Cyclonic
	Mature bow echo	9	Cyclonic
10 Jun 2003	Cellular	4	2 cyclonic, 2 possible couplets
	Early bow echo	5	Cyclonic
	Mature bow echo	1	Cyclonic
6 Jul 2003	Mature bow echo	5	Cyclonic and couplets

radar data were analyzed at the time of mesovortex genesis to determine if the circulations were cyclonic or produced as a couplet. No anticyclonic-only mesovortices were observed in these three cases. The mesovortices were further categorized according to the stage of convective system evolution, similar to the control run herein. The results are presented in Table 1. Beginning with the 29 June 1998 case, all of the mesovortices were cyclonic and formed during the early bow echo and mature bow echo stages. No couplets were observed. The 10 June 2003 case produced mesovortices during all three stages of evolution. Cyclonic mesovortices and possible couplets were observed during the cellular stage whereas cyclonic-only mesovortices were observed later during the early and mature bow echo stages. The results of 29 June 1998 and 10 June 2003 highlight the potential role that the cyclonic mesovortex genesis mechanism discussed herein may play in producing observed mesovortices.

The last case was the 6 July 2003 bow echo. Unlike the previous two cases, vortex couplets were observed with this event (Table 1). Indeed, Wakimoto et al. (2006b) observed couplets in dual-Doppler airborne radar data and attributed their formation to mechanically generated downdrafts tilting cold-pool vortex lines. This mechanism is similar to the one discussed by Trapp and Weisman (2003) and resulted in the anticyclonic circulation formed to the north of the cyclonic vortex.

Intrigued by the dual-Doppler radar observations of couplets in the 6 July 2003 bow echo, the WRF model was used to create a quasi-idealized simulation of the 6 July 2003 event. The model set up was similar to the control with two exceptions. First, the sounding used to initialize the model was launched from Omaha, Nebraska, at 0000 UTC 6 July 2003 and represents well

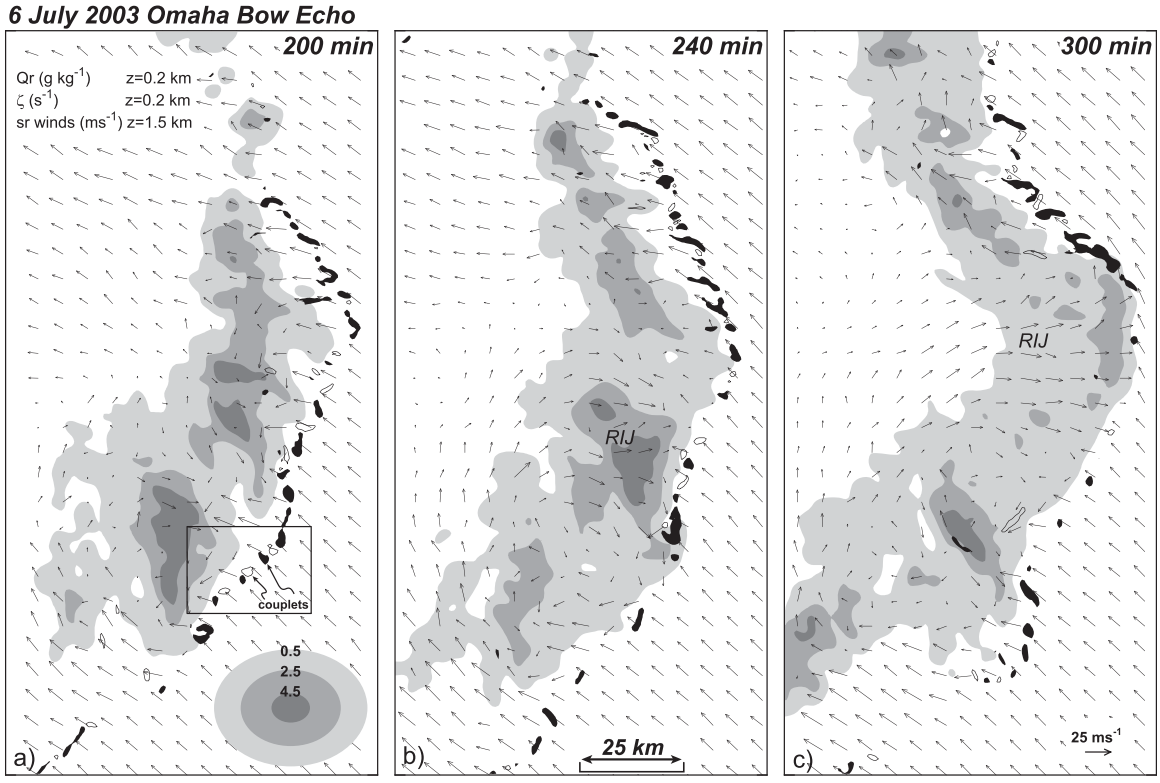

FIG. 13. Evolution of the 6 Jul 2003 simulation at 200, 240, and 300 min. Rainwater mixing ratio (g kg^{-1}) is shaded gray. Locations of cyclonic mesovortices where the vertical vorticity is greater than 7.5×10^{-3} s^{-1} are filled in black. The thin black contours are locations of anticyclonic mesovortices having vertical vorticity values less than -7.5×10^{-3} s^{-1}. Storm relative winds (m s^{-1}) at 1.5 km are plotted at all times. The box in (a) represents the domain shown in Fig. 14a.

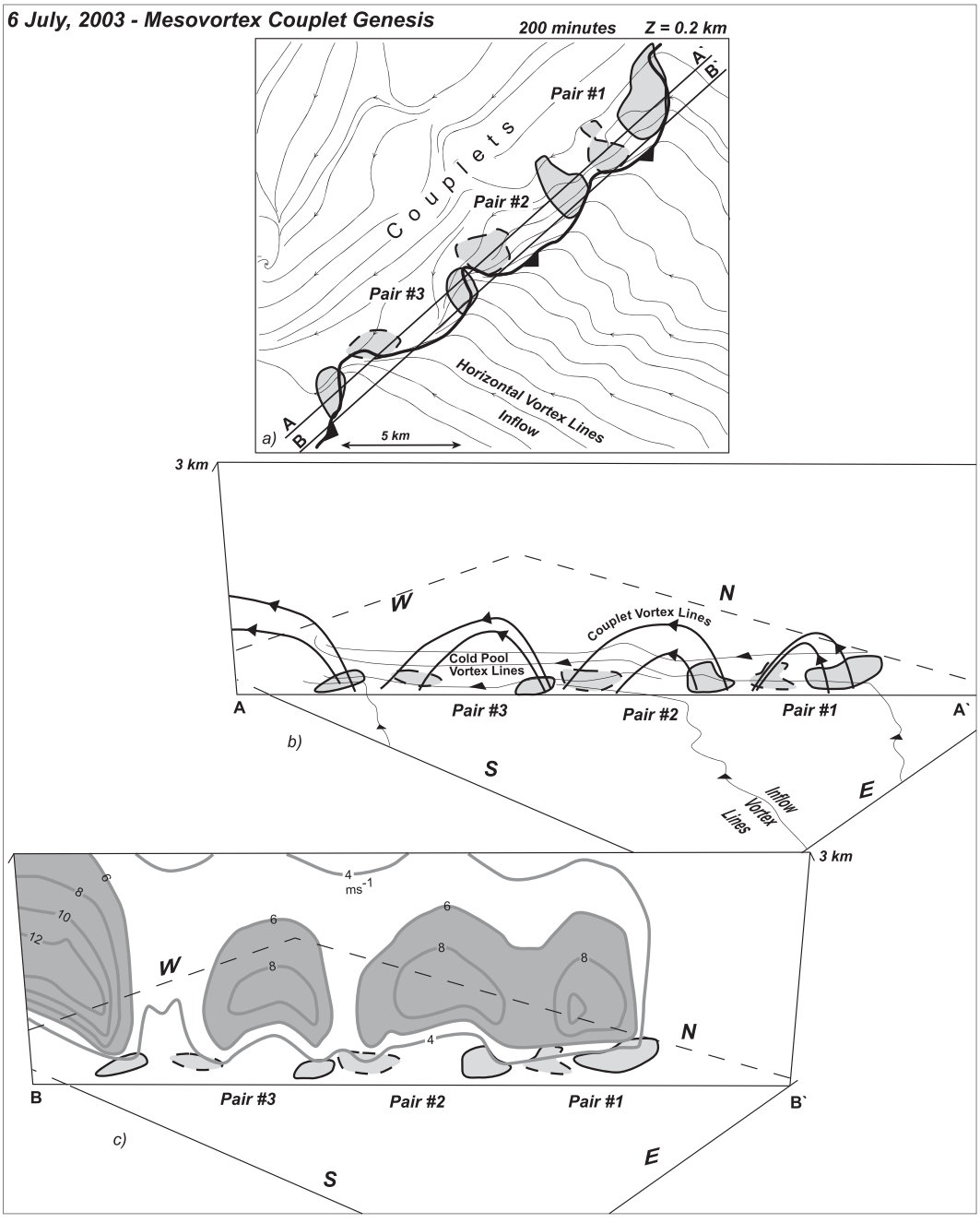

FIG. 14. Simulation of the 6 Jul 2003 Omaha bow echo event shown in Fig. 13. (a) The domain location is shown in Fig. 13a. All fields are the same as in Fig. 8.

the environment within which the bow echo propagated. Second, convection was initiated with four thermal bubbles oriented in a southwest–northeast manner, consisent with the line orientation of the developing convective system.

The simulation, shown in Fig. 13, produced a bow echo that evolved in a manner similar to that documented in the radar data. While the convective system had not yet developed into a bow echo at 200 min (Fig. 13a), a number mesovortex couplets were observed along the gust front. Couplets were also observed at 240 min (Fig. 13b) as the system-scale RIJ began to form. As the system matured (Fig. 13c), the number of anticyclonic mesovortices decreased, consistent with the observations of Trapp and Weisman (2003) who showed that convergence of planetary vorticity had a measurable affect in strengthening (weakening) cyclonic (anticyclonic) mesovortices.

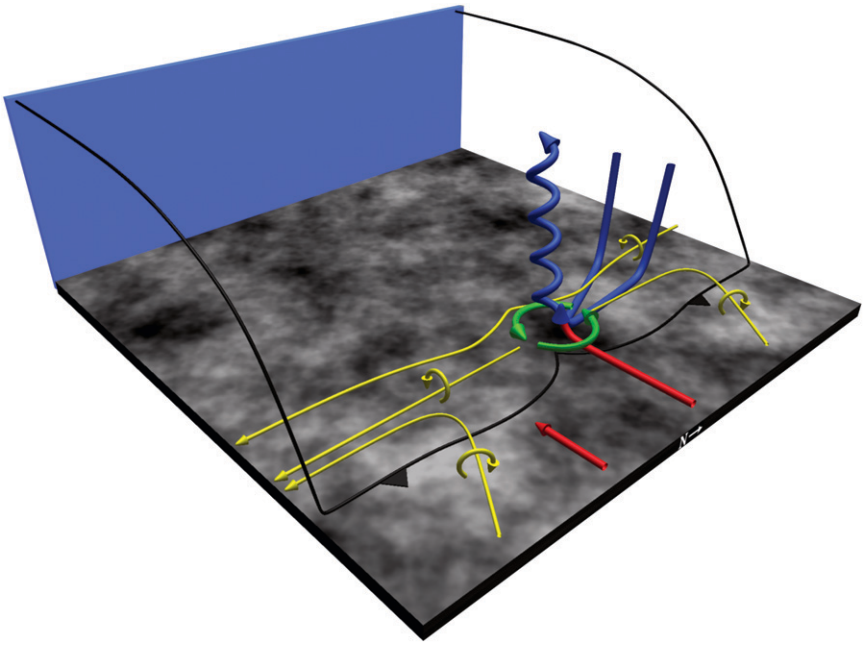

FIG. 15. Schematic diagram of cyclonic-only mesovortex genesis. Vortex lines (gold), inflow and updraft (red), and downdraft (blue) are all depicted. The thick green arrow represents the mesovortex. The gust front position is shown in black.

A closer examination of the mesovortex couplets in Fig. 13a is shown in Fig. 14a. Consistent with the control run discussed herein, mesovortex couplets formed on the bow echo gust front with the cyclonic member located to the north. As in the control run, cold-pool vortex lines passed through the couplets from northeast to southwest, shown in Figs. 14a,b. In the vertical cross section passing through the couplets (Fig. 14b), the vortex lines arched upward with positive vertical vorticity located to the north. The vortex lines were tilted upward by localized updraft maxima located between the positive and negative vertical vorticity maximum (Fig. 14c). Thus, the couplets observed in the 6 July 2003 bow echo simulation may have formed from the upward tilting of cold-pool vortex lines by localized updraft maxima along the gust front. While this result is the same as that observed in the control run, it is different than what was shown by Wakimoto et al. (2006b) and in a real-data simulation of the same event by Wheatley and Trapp (2008). This discrepency in genesis mechanisms is discussed further in the next section.

5. Summary, discussion, and conclusions

The genesis mechanisms of mesovortices formed within bow echoes has been presented. In particular, the analysis focused on a quasi-idealized simulation of the 10 June 2003 Saint Louis bow echo documented by Atkins et al. (2005). The Saint Louis bow echo produced a number of mesovortices, many produced surface wind damage.

Two different genesis mechanisms were identified. As schematically shown in Fig. 15, the first describes the genesis of cyclonic vortices that were observed to form during nearly all stages of convective system evolution. Parcels that populated the developing mesovortex originated from two different regions. The first was high θ_e inflow air at low levels. The other was low θ_e air that originated within convective-scale downdrafts or the RIJ, when present. Analysis of the vertical vorticity equation showed that parcels descending within the downdraft acquired horizontal vorticity, which was subsequently tilted by the updraft along the gust front. The horizontal vorticity was solenoidally generated by the baroclinc zone across the gust front. The updraft further amplified the vertical vorticity through stretching. The genesis of the cyclonic mesovortices was also investigated through analysis of circulation around a material surface surrounding the mesovortex. This analysis confirmed the two source regions of air feeding the vortex. It was also shown that the circulation around the material surface increased with time as it converged into the final position surrounding the mesovortex. The increased circulation was attributed to the buoyancy distribution around the material surface and confirmed that the mesovortex was formed by the tilting of horizontal horizontal vortex lines encompassed by the material

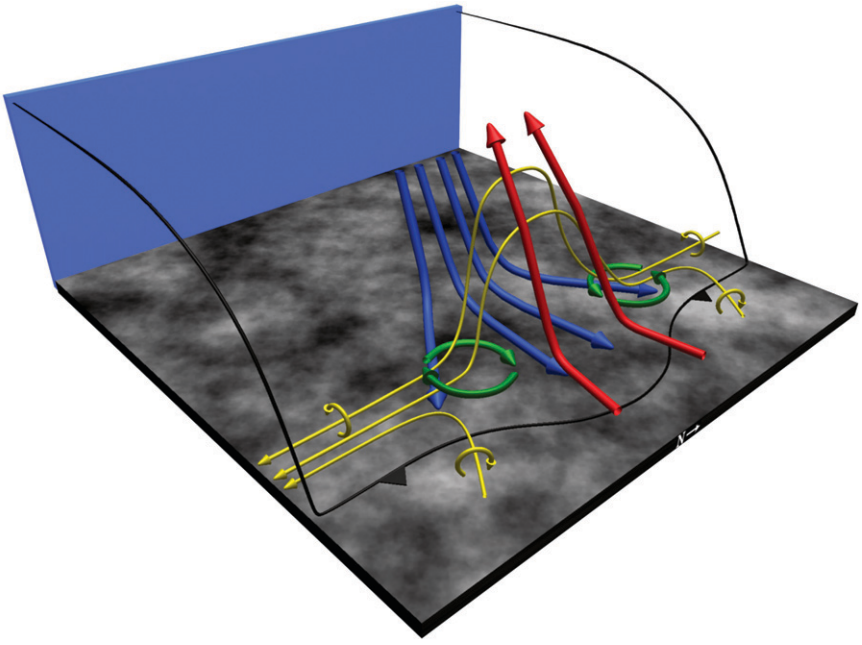

FIG. 16. Schematic diagram of cyclonic–anticyclonic mesovortex genesis. Vortex lines (gold), inflow and updraft (red), and downdraft (blue) are all depicted. The thick green arrow represents the mesovortices. Gust front position is shown in black.

surface. This mechanism is similar to what has been desribed by previous investigators for the genesis of low-level mesocyclones observed within supercell thunderstorms (e.g., Rotunno and Klemp 1985; Davies-Jones and Brooks 1993).

The second mesovortex genesis mechanism, schematically illustrated in Fig. 16, produced couplets with the cyclonic vortex located to the north of the anticyclonic member. This mechanism was observed predominantly during the early bow echo stage. The mechanism was elucidated through analysis of vortex lines passing through the couplets. Along and just behind the north–south-oriented gust front, vortex lines were oriented to the south. Localized updrafts tilted the initially horizontal cold-pool vortex lines upward, creating arches of vortex lines centered on the updraft. Thus, cyclonic (anticyclonic) vertical vorticity was produced on the northern (southern) side of the updraft. The localized updraft maximum was generated by a convective-scale downdraft that produced outflow. The outflow locally accelerated the gust front outward, producing the updraft maximum.

The generation of vertical vorticity couplets as shown in Fig. 16 has been discussed elsewhere in the literature. This mechanism was illustrated by Weisman and Davis (1998) to explain the genesis of midlevel line-end vortices that form on the ends of squall lines. The scale of the vortices was much larger than mesovortices formed on the gust front presumably due to the larger scale of the system updraft that was tilting the cold-pool vortex lines. Moreover, Markowski et al. (2008) have recently shown that arching vortex lines were produced in the vicinity of supercell hook echoes. By examining dual-Doppler radar data, their analysis showed that the arching vortex lines pass through the cyclonic low-level mesocyclone within the hook echo and a broad area of anticyclonic vertical vorticity usually located to the south or southwest. The data strongly suggested that the horizontal vortex lines were baroclinically generated and that updraft tilted them to form the vortex line arches.

An analysis was undertaken to determine if the cyclonic-only mesovortices were produced by a shearing instability. By comparing the observed mesovortex genesis spacing to that predicted by linear theory, it was concluded that shearing instability was likely not active in creating mesovortices.

A comparison of the mesovortex genesis mechanisms reported herein was made with available observations of mesovortices formed within damaging bow echoes observed during the warm season. Three events previously reported in the literature were studied. They included the 29 June 1998 (Atkins et al. 2004), 10 June 2003 (Atkins et al. 2005), and 6 July 2003 (Wakimoto et al. 2006a,b; Wheatley et al. 2006) events. Analysis of single-Doppler radar data suggested that cyclonic-only mesovortices formed during the 29 June 1998 and 10 June 2003

TABLE 2. Preferred mesovortex genesis mechanism observed in all the sensitivity runs shown in Part I. The 6 Jul 2003 simulation is also included. Lin refers to the Lin et al. (1983) ice microphysics scheme and **ΔU** is the wind velocity change over the respective depth.

Expt type	Depth of **ΔU** (km)	**ΔU** (m s^{-1})	Microphysics scheme/Coriolis	Preferred mesovortex genesis mechanism
Control	2.5, 5.0	18, 22	Lin/1 $\times$ 10^{-4} s^{-1}	Couplets early–cyclonic mature
Low-level Shear	2.5	10	Lin/1 $\times$ 10^{-4} s^{-1}	Couplets
		30	Lin/1 $\times$ 10^{-4} s^{-1}	Cyclonic
Midlevel Shear	5.0	15	Lin/1 $\times$ 10^{-4} s^{-1}	Couplets
		20	Lin/1 $\times$ 10^{-4} s^{-1}	Couplets
		30	Lin/1 $\times$ 10^{-4} s^{-1}	Cyclonic
Coriolis	Same as control	Same as control	Lin/1 $\times$ 10^{-6} s^{-1}	Couplets and cyclonic
			Lin/2 $\times$ 10^{-4} s^{-1}	Couplets early–cyclonic mature
Cold-pool strength	Same as control	Same as control	Kessler: evaporation rate = 100%/1 $\times$ 10^{-4} s^{-1}	Couplets early–cyclonic mature
			Evaporation rate = 50%/1 $\times$ 10^{-4} s^{-1}	Cyclonic
			Evaporation rate = 25%/1 $\times$ 10^{4} s^{-1}	Cyclonic
6 Jul 2003	2.0, 6.0	11, 24	Lin/1 $\times$ 10^{-4} s^{-1}	Couplets

bow echo events, thus providing supporting evidence that the cyclonic mesovortex genesis mechanism shown in Fig. 15 may be occurring in observed bow echoes.

The results presented by Wakimoto et al. (2006b) showed mesovortex couplets formed by dowward tilting of cold-pool vortex lines by mechanically forced downdrafts. Wheatley and Trapp (2008) identified downward tilting of cold-pool vortex lines by precipitation-induced downdrafts as the mesovortex couplet mechanism. A quasi-idealized simulation of this event was performed to further study the genesis of the mesovortex couplets. Similar to the process shown in Fig. 16, the simulated couplets formed through the upward tilting of cold-pool vortex lines by a localized updraft maximum. The discrepency in mesovortex genesis mechanisms for the 6 July 2003 case as discussed by Wakimoto et al. (2006b), Wheatley and Trapp (2008), and herein is not well understood.

In Part I, it was shown that mesovortex strength depended upon the environmental shear, Coriolis forcing, and cold-pool strength. As shown in Table 2, the preferred mesovortex genesis mechanism also appears to depend upon the aforementioned parameters. Couplets were commonly observed in the weaker low- and midlevel shear environments. This includes the 6 July 2003 simulation where 11 m s^{-1} of shear was observed in the lowest 2 km. Thus, while the 6 July 2003 simulation results reported herein of mesovortex genesis appear to be different than those discussed by Wakimoto et al. (2006b) and Wheatley and Trapp (2008), they are consistent with the other weak shear simulations analyzed in this study. As the shear magnitude increases to moderate values (control), couplets were observed in the early bow echo stages whereas cyclonic mesovortices dominated in the mature stage. As the shear strengthens further, the cyclonic mesovortex mechanism dominated.

An important conclusion of this study is that there may be more than one process that produces mesovortices within bow echoes. Future research should focus on collecting high-resolution observations of mesovortices. This could be accomplished with mobile-Doppler radars that would provide rapid updates of the evolving wind field surrounding a developing mesovortex.

Acknowledgments. Research results presented in this paper were supported by the National Science Foundation under Grant ATM-0630445 and Vermont EPSCoR EPS-0236976. Model graphics were created by the Read/Interpolate/Plot (RIP) software package created by Mark T. Stoelinga. Comments by three anonymous reviewers on an earlier version of the manuscript were greatly appreciated.

REFERENCES

Adlerman, E. J., and K. K. Droegemeier, 2002: Sensitivity of numerically simulated cyclic mesocyclogenesis to variations in model physical and computational parameters. *Mon. Wea. Rev.,* **130,** 2671–2691.

Arnott, N. R., Y. P. Richardson, J. M. Wurman, and E. M. Rasmussen, 2006: Relationship between a weakening cold front, misocyclones, and cloud development on 10 June 2002 during IHOP. *Mon. Wea. Rev.,* **134,** 311–335.

Atkins, N. T., and M. St. Laurent, 2009: Bow echo mesovortices. Part I: Processes that influence their damaging potential. *Mon. Wea. Rev.,* **137,** 1497–1513.

——, J. M. Arnott, R. W. Przybylinski, R. A. Wolf, and B. D. Ketcham, 2004: Vortex structure and evolution within bow echoes. Part I: Single-Doppler and damage analysis of the 29 June 1998 derecho. *Mon. Wea. Rev.,* **132,** 2224–2242.

——, C. S. Bouchard, R. W. Przybylinski, R. J. Trapp, and G. Schmocker, 2005: Damaging surface wind mechanism within the 10 June 2003 Saint Louis bow echo during BAMEX. *Mon. Wea. Rev.,* **133,** 2275–2296.

Batchelor, G. K., 1967: *An Introduction to Fluid Dynamics*. Cambridge University Press, 615 pp.

Burgess, D. W., and B. F. Smull, 1990: Doppler radar observations of a bow echo associated with a long-track severe windstorm. Preprints, *16th Conf. on Severe Local Storms,* Kananaskis Park, Alberta, Canada, Amer. Meteor. Soc., 203–208.

Carbone, R. E., 1982: A severe frontal rainband. Part I: Stormwide hydrodynamic structure. *J. Atmos. Sci.,* **39,** 258–279.

Davies-Jones, R. P., and H. E. Brooks, 1993: Mesocyclogenesis from a theoretical perspective. *The Tornado: Its Structure, Dynamics, Prediction, and Hazards, Geophys. Monogr.,* Vol. 79, Amer. Geophys. Union, 105–114.

Eliassen, A., and E. Kleinschmidt, 1957: Dynamic meteorology. *Handbuch der Physik,* Vol. 58, Springer-Verlag, 1–154.

Forbes, G. S., and R. M. Wakimoto, 1983: A concentrated outbreak of tornadoes, downbursts and microbursts, and implications regarding vortex classification. *Mon. Wea. Rev.,* **111,** 220–236.

Fujita, T. T., 1978: Manual of downburst identification for project Nimrod. Satellite and Mesometeorology Research Paper 156, Dept. of Geophysical Sciences, University of Chicago, 104 pp. [NTIS PB-286048.]

Funk, T. W., K. E. Darmofal, J. D. Kirkpatrick, V. L. DeWald, R. W. Przybylinski, G. K. Schmocker, and Y.-J. Lin, 1999: Storm reflectivity and mesocyclone evolution associated with the 15 April 1994 squall line over Kentucky and southern Indiana. *Wea. Forecasting,* **14,** 976–993.

Johns, R. H., and W. D. Hirt, 1987: Derechos: Widespread convectively induced wind-storms. *Wea. Forecasting,* **2,** 32–49.

Jorgensen, D. P., and B. F. Smull, 1993: Mesovortex circulations seen by airborne Doppler radar within a bow-echo mesoscale convective system. *Bull. Amer. Meteor. Soc.,* **74,** 2146–2157.

Klimowski, B. A., R. Przybylinski, G. Schmocker, and M. R. Hjelmfelt, 2000: Observations of the formation and early evolution of bow echoes. Preprints, *20th Conf. on Severe Local Storms,* Orlando, FL, Amer. Meteor. Soc., 44–47.

Lee, B. D., and R. B. Wilhelmson, 1997: The numerical simulation of non-supercell tornadogenesis. Part I: Initiation and evolution of pretornadic misocyclone and circulations along a dry outflow boundary. *J. Atmos. Sci.,* **54,** 32–60.

Lin, Y.-L., R. D. Farely, and H. D. Orville, 1983: Bulk parameterization of a snow field in a cloud model. *J. Climate Appl. Meteor.,* **22,** 1065–1092.

Markowski, P., E. Rasmussen, J. Straka, R. Davies-Jones, Y. Richardson, and R. J. Trapp, 2008: Vortex lines within low-level mesocyclones obtained from pseudo-Doppler radar observations. *Mon. Wea. Rev.,* **136,** 3513–3535.

Marquis, J. N., Y. P. Richardson, and J. M. Wurman, 2007: Kinematic observations of misocyclones along boundaries during IHOP. *Mon. Wea. Rev.,* **135,** 1749–1768.

Miles, J. W., and L. N. Howard, 1964: Note on heterogeneous shear flow. *J. Fluid Mech.,* **20,** 331–336.

Mueller, C. K., and R. E. Carbone, 1987: Dynamics of a thunderstorm outflow. *J. Atmos. Sci.,* **44,** 1879–1898.

Murphey, H. V., R. M. Wakimoto, C. Flamant, and D. E. Kingsmill, 2006: Dryline on 19 June 2002 during IHOP. Part I: Airborne Doppler and LEANDRE II analyses of the thin line structure and convection initiation. *Mon. Wea. Rev.,* **134,** 406–430.

Orlanski, I., 1975: A rational subdivision of scales for atmospheric processes. *Bull. Amer. Meteor. Soc.,* **56,** 527–530.

Przybylinski, R. W., 1995: The bow echo: Observations, numerical simulations, and severe weather detection methods. *Wea. Forecasting,* **10,** 203–218.

——, G. K. Schmocker, and Y.-J. Lin, 2000: A study of storm and vortex morphology during the intensifying stage of severe wind mesoscale convective systems. Preprints, *20th Conf. on Severe Local Storms,* Orlando, FL, Amer. Meteor. Soc., 173–176.

Rotunno, R., and J. B. Klemp, 1985: On the rotation and propagation of simulated supercell thunderstorms. *J. Atmos. Sci.,* **42,** 271–292.

Schmidt, J. M., and W. R. Cotton, 1989: A high plains squall line associated with severe surface winds. *J. Atmos. Sci.,* **46,** 281–302.

Schmocker, G. K., R. W. Przybylinski, and E. N. Rasmussen, 2000: The severe bow echo event of 14 June 1998 over the mid-Mississippi Valley region: A case of vortex development near the intersection of a preexisting boundary and a convective line. Preprints, *20th Conf. on Severe Local Storms,* Orlando, FL, Amer. Meteor. Soc., 169–172.

Skamarock, W. C., M. L. Weisman, and J. B. Klemp, 1994: Three-dimensional evolution of simulated long-lived squall lines. *J. Atmos. Sci.,* **51,** 2563–2584.

——, J. B. Klemp, J. Dudhia, D. O. Gill, D. M. Barker, W. Wang, and J. G. Powers, 2005: A description of the Advanced Research WRF version 2. NCAR Tech. Note TN-468-STR, 88 pp. [Available from NCAR, P.O. Box 3000, Boulder, CO 80307.]

Trapp, R. J., and B. H. Fiedler, 1995: Tornado-like vortexgenesis in a simplified numerical model. *J. Atmos. Sci.,* **52,** 3757–3778.

——, and M. L. Weisman, 2003: Low-level mesovortices within squall lines and bow echoes. Part II: Their genesis and implications. *Mon. Wea. Rev.,* **131,** 2804–2823.

Wakimoto, R. M., 1983: The West Bend, Wisconsin, sStorm of 4 April 1981: A problem in operational meteorology. *J. Climate Appl. Meteor.,* **22,** 181–189.

——, and J. W. Wilson, 1989: Non-supercell tornadoes. *Mon. Wea. Rev.,* **117,** 1113–1140.

——, H. V. Murphey, A. Nester, D. P. Jorgensen, and N. T. Atkins, 2006a: High winds generated by bow echoes. Part I: Overview of the Omaha bow echo 5 July 2003 storm during BAMEX. *Mon. Wea. Rev.,* **134,** 2793–2812.

——, ——, C. A. Davis, and N. T. Atkins, 2006b: High winds generated by bow echoes. Part II: The relationship between the mesovortices and damaging straight-line winds. *Mon. Wea. Rev.,* **134,** 2813–2829.

Weisman, M. L., 1993: The genesis of severe, long-lived bow echoes. *J. Atmos. Sci.,* **50,** 645–670.

——, and C. Davis, 1998: Mechanisms for the generation of mesoscale vortices within quasi-linear convective systems. *J. Atmos. Sci.,* **55,** 2603–2622.

——, and R. J. Trapp, 2003: Low-level meso-vortices within squall lines and bow echoes. Part I: Overview and dependence on environmental shear. *Mon. Wea. Rev.,* **131,** 2779–2803.

Wheatley, D. M., and R. J. Trapp, 2008: The effect of mesoscale heterogeneity on the genesis and structure of mesovortices within quasi-linear convective systems. *Mon. Wea. Rev.,* **136,** 4220–4241.

——, ——, and N. T. Atkins, 2006: Radar and damage analysis of severe bow echoes observed during BAMEX. *Mon. Wea. Rev.,* **134,** 791–806.